Mechatronics 96 (2023) 103070

Contents lists available at ScienceDirect

Mechatronics

journal homepage: www.elsevier.com/locate/mechatronics

An estimation of triaxial forces from normal stress tactile sensor arrays ☆

María L. Pinto-Salamanca [a,b,*], Julián Castellanos-Ramos [b], Wilson J. Pérez-Holguín [a], José A. Hidalgo-López [b]

[a] Doctorado en Ingeniería énfasis en Ingeniería Electrónica Universidad Pedagógica y Tecnológica de Colombia UPTC, Sogamoso, 152211, Colombia
[b] Departamento de Electrónica, Universidad de Málaga, Málaga, 29071, Spain

ARTICLE INFO

Keywords:
Contact forces reconstruction
Model-driven
Normal stress
Tactile sensor array

ABSTRACT

This work proposes a new method to find an optimal solution of the inverse problem of the Boussinesq equation for ill-posed problems, applicable in the reconstruction of triaxial forces for processing contact data in tactile decoding systems. This paper focuses on the estimation of triaxial forces from normal stress tactile sensor arrays on flat non-deformable surfaces for single static contacts. This method estimates a triaxial force vector on the sensor coverage surface for each stress value from the relation between the stress data and the applied normal and tangential contact forces. The main contribution of this work consists of a new procedure for estimating contact forces simplifying both arithmetic operations and the optimization process used. Because of this, obtaining a force estimation has a predictable computation time, which makes this new method an attractive solution for implementation in hardware-based real-time tactile sensing systems. The verification process was conducted using a Finite Element Analysis (FEA) as a reference. When testing tactile sensors in a range of sizes and resolutions for piezoelectric and piezoresistive technologies, a maximum estimation error of 10.93% was obtained, including errors due to the array discretization.

1. Introduction

Tactile sensing systems can improve quality of life by enabling artificial replication of the human sense of touch. Due to its importance, the scientific community has spent more than three decades seeking to replicate complex somatosensory systems through the definition of behavioral models, the development of specialized sensors, and the generation of software and hardware to capture, transmit and process contact events [1,2].

Tactile sensing systems are composed of three main stages known as the contact information capture subsystem (comprising continuous and discrete tactile sensors) [3], the electronic interface subsystems (in charge of acquiring, transmitting, and preprocessing contact data) [4,5], and the decoding subsystem (to identify the properties, types, patterns and modalities of the contact events) [6]. Within the last one, reconstructing contact forces plays a key role in describing contact phenomena since it is responsible for detecting the distribution of forces and their temporal evolution [7].

In the robotics field, reconstructing contact forces helps us to understand and plan the interactions of the robot with the environment [8], and to adequately perform applications such as slip detection and robotic grasping [9,10], shape recognition [11], and human–robot interaction [12]. Forces reconstruction is further used to implement robotic skin [13], wearable robots [14], soft robots [15], and robotic hands [16]. In the field of tactile sensors, it is relevant when designing soft sensors [17], large-scale tactile sensors [18] and vision-based integration sensors [19]. In the biomedical field, it is also important for developing haptic devices [20,21], medical measurements [22,23], wearable biosensing [24], and others.

Reconstructing contact forces depends on a set of variables such as the contact scenario, sensor data, contact mechanics, and the estimation approach. The reconstruction method implemented should simultaneously report the magnitude, forces location, and direction associated with the contact [25]. Furthermore, it must comply with the rules established in [26] for evaluating tactile sensing models, including: (i) the generalization criteria (the contact reconstruction should not assume any a priori model of the object in contact), (ii) efficiency (force reconstruction time should be predictable), and (iii) scalability (the reconstruction solution should be scalable to different contact area sizes).

The aforementioned variables tend to increase the complexity of the reconstruction process, which poses a challenge for the development

☆ This paper was recommended for publication by Associate Editor Kai-Tai Song.

* Corresponding author at: Doctorado en Ingeniería énfasis en Ingeniería Electrónica Universidad Pedagógica y Tecnológica de Colombia UPTC, Sogamoso, 152211, Colombia.
E-mail address: marialuisa.pinto@uptc.edu.co (M.L. Pinto-Salamanca).

https://doi.org/10.1016/j.mechatronics.2023.103070
Received 9 December 2022; Received in revised form 8 August 2023; Accepted 14 September 2023
Available online 4 October 2023

of large-area, high-density sensors [18], and implementing real-time multi-axial force estimation systems independent of the sensing area and transduction technology [27]. Efforts to achieve real-time operation involve optimizing the reconstruction model and designing data reading and processing hardware capable of meeting strict system time limits.

Contact force data capture is performed using continuous or discrete contact media, depending on the sensor technology. Examples of continuous sensors include vision based [11], magnetostrictive [10], biomimetic fingertip [20], and Hall effect [9] technologies. For discrete contact media, there are sensor arrays based on optoelectronics [12,13,16,17,28,29], piezoelectric [14,19,30,31], magnetic composites [15], nanocomposites [21,24], inductive [23], capacitive [32–34], force–torque [35], and force-sensitive devices [25,36–38].

Several sensor arrays directly measure normal forces [25,31,33], normal and shear forces [38,39], triaxial forces [7,12,28,35,40], or six-axis contact forces [16,17,30,41]. All these tactile sensor arrays enable force measurement in large sensing areas along with static [7,35], and dynamic [12,16,28,29] contact events processing. In this context, multiaxial force estimate becomes the bottleneck in the design of tactile decoding subsystems, since multiaxial contact sensors typically employ expensive transduction technologies, have complex electronics, and poor commercial availability.

Conversely, despite the low cost and wide availability of normal stress tactile sensor arrays, there are few works reported in the literature that use them to obtain information on triaxial forces. These works include model-driven approaches for modeling triaxial forces [7], and mixed strategies for normal force definition and validation stages [32].

In [7], the authors perform a forces triaxial reconstruction regardless of the transducer employed, to model single static contacts on non-deformable flat surfaces. Such a work proposes solving the inverse problem for the Boussinesq equation for an elastic half-space [42] using inherent physical considerations to the solution of an ill-conditioned problem by means of the Moore–Penrose pseudo-inverse matrix [43]. Although that model meets the generalization and scalability rules stated in [26], it does not clearly establish the execution time predictability. In addition, such a model requires the calculation of a multivariable optimization function with high computational complexity.

Alternatively, this work proposes a novel solution to the ill-posed inverse Boussinesq problem using the same range of physical assumptions proposed in [7] but reinterpreting their meaning. Thanks to this, on the one hand, the complexity of the optimization process necessary to obtain the best triaxial reconstruction is reduced. On the other hand, the arithmetic operations at each step of the optimization process are simpler. Our method offers improvements for future real-time implementations in hardware targeted at modeling non-deformable contacts on flat surfaces, complying in addition with the generalization, scalability and efficiency rules proposed in [26].

2. Contact forces from a tactile sensor array

The tactile sensing system considered in this work consists of an array of normal stress sensing units (taxels) fixed on a rigid surface, coated with an elastomer layer of thickness h. The tactile force applied on the outer surface of the elastomer, f_i, is received by the taxels as pressure on their upper side, T_j, see Fig. 1. Based on the theory of elasticity, it is possible to find the normal stress at any taxel from the surface force distribution. The Green function of this problem for an elastic half-space is known as the Boussinesq equation [44,45]. In the case of linear elasticity, when force distribution is discretized into an array of m point forces and m taxels ($m = M \times N$, where M is the number of rows and N is the number of columns in the tactile sensor array), a superposition of the Boussinesq equations can be used as an approximation to find the stress vector,

$$b = C \cdot f \tag{1}$$

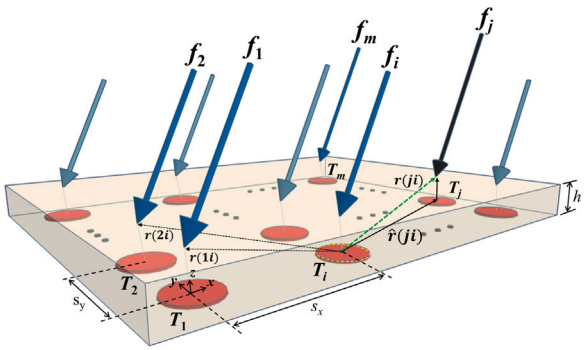

Fig. 1. Contact force reconstruction for a tactile sensor array. T_1 to T_m are the taxels producing the stress data b_z, while f_1 to f_m are the applied force vectors.

where $b = [b_x\ b_y\ b_z]^T$ is a triaxial stress vector of size $3m \times 1$ and $f = [f_x\ f_y\ f_z]^T$ is a triaxial force vector of size $3m \times 1$ estimated at the same $XY-$coordinates of taxels on the sensor cover layer. The square matrix C depends on the distances $r(ji)$ between the coordinates of the taxel ith ($i = 1, \ldots, m$) and the force jth ($j = 1, \ldots, m$), along with the vector $\hat{r}(ji)$, which is the projection of vector $r(ji)$ on the $XY-$plane with coordinates $(\hat{r}(ji)_x, \hat{r}(ji)_y)$ [42]. The $r(ji)$ and $\hat{r}(ji)$ vectors depend on the taxels resolution (s_x, s_y) and the sensor cover thickness, h, see Fig. 1.

Since the taxels location in the sensor array is fixed and known, C becomes a constant matrix. When C is a non-singular matrix, the Boussinesq equation provides the force vector on the sensor cover surface from the stress data b,

$$f = C^{-1} \cdot b \tag{2}$$

This work focuses on tactile sensors providing only the normal stress value b_z for each discrete taxel (without including tangential stress data), as usual in tactile sensor arrays. In that case, the Boussinesq equation becomes an ill-posed system such that,

$$b_z = A \cdot \begin{bmatrix} f_x \\ f_y \\ f_z \end{bmatrix} \tag{3}$$

where A is a matrix of size $m \times 3m$ given by,

$$A = \begin{bmatrix} C_{31} & C_{32} & C_{33} \end{bmatrix} \tag{4}$$

and C_{31}, C_{32}, and C_{33} are $m \times m$ submatrices of C described as,

$$\begin{bmatrix} C_{31} & C_{32} & C_{33} \end{bmatrix}^T = \begin{bmatrix} C_0 \cdot \hat{r}(ji)_x \\ C_0 \cdot \hat{r}(ji)_y \\ C_0 \cdot h \end{bmatrix} \tag{5}$$

with $C_0 = (3h^2)/(2\pi(\hat{r}(ji)^2 + h^2)^{5/2})$.

The Moore–Penrose pseudo-inverse matrix is defined as,

$$A\dagger = A^T \left(AA^T\right)^{-1} = \begin{bmatrix} A\dagger_1 \\ A\dagger_2 \\ A\dagger_3 \end{bmatrix} \tag{6}$$

with $A\dagger_1$, $A\dagger_2$, and $A\dagger_3$ being matrices of size $m \times m$, that could be used to parametrically solve the ill-posed system shown in Eq. (3).

It is known that all possible solutions of Eq. (3) have the form,

$$f = A\dagger b_z + (I - A\dagger A)\, w \tag{7}$$

where w is an arbitrary determined weight vector of size $3m \times 1$. It should be noted that the physics of the problem may constrain the w vector composition. In particular, [7] proposes a w vector that assumes a tangential forces distribution proportional to the normal forces distribution, such that,

$$w = \begin{bmatrix} w_x \\ w_y \\ w_z \end{bmatrix} = \begin{bmatrix} \mu_x |w_z| \\ \mu_y |w_z| \\ w_z \end{bmatrix} \tag{8}$$

with w_z a vector made up of the negative values of the solution of the inverse Boussinesq problem considering only the application of normal forces,

$$w_z = \begin{cases} C_{33}^{-1} \cdot b_z & ;\left(C_{33}^{-1} \cdot b_z\right)(i) < 0 \\ 0 & ;\text{other case} \end{cases} \tag{9}$$

and μ_x and μ_y are two continuous scalar variables in the range $[-1, 1]$.

Given Eqs. (6), (8) and (9), Eq. (7) can be written as,

$$\begin{bmatrix} f_x & f_y & f_z \end{bmatrix}^T = \begin{bmatrix} A\dagger_1 b_z - A\dagger_1 C_{33} w_z + \mu_x \left(|w_z| - A\dagger_1 C_{31}|w_z|\right) \\ +\mu_y \left(-A\dagger_1 C_{32}|w_z|\right) \\ \\ A\dagger_2 b_z - A\dagger_2 C_{33} w_z + \mu_x \left(-A\dagger_2 C_{31}|w_z|\right) \\ +\mu_y \left(|w_z| - A\dagger_2 C_{32}|w_z|\right) \\ \\ A\dagger_3 b_z + w_z - A\dagger_3 C_{33} w_z + \mu_x \left(-A\dagger_3 C_{31}|w_z|\right) \\ +\mu_y \left(-A\dagger_3 C_{32}|w_z|\right) \end{bmatrix} = \begin{bmatrix} a_{10} + \mu_x a_{11} + \mu_y a_{12} \\ a_{20} + \mu_x a_{21} + \mu_y a_{22} \\ a_{30} + \mu_x a_{31} + \mu_y a_{32} \end{bmatrix} \tag{10}$$

where a_{pq} are vectors of size $m \times 1$ that depend on the submatrices C_{31}, C_{32}, and C_{33}, the matrix $A\dagger$, and the vector w_z (for instance, $a_{10} = A\dagger_1 b_z - A\dagger_1 C_{33} w_z$). The problem is therefore defined as a system of $3m$ linear functions with $3m + 2$ unknown variables (f_x, f_y, f_z, μ_x, and μ_y).

To solve this undetermined system, [7] poses finding variables μ_x and μ_y using an objective function $\Pi = \Pi_1 \cdot \Pi_2 \cdot \Pi_3$ which simultaneously fulfills three physical constraints imposed on the problem: (i) considering contacts with compressive normal forces, (ii) tangential and normal forces similarly distributed over the contact area, and (iii) no pinch.

The iterative search for μ_x and μ_y ends when it is found a combination of these values that maximizes the Π function. However, the computational complexity of this process must be carefully analyzed, considering that for each step: (i) $\Pi_1(f_z, \mu_x, \mu_y)$ depends on $m + 2$ variables, (ii) $\Pi_2(f_x, f_y, \mu_x, \mu_y)$ depends on $2m + 2$ variables, and (iii) $\Pi_3(f_x, f_y, \mu_x, \mu_y, d_1, d_2)$ depends on $4m + 2$ variables, where d_1 and d_2 are vectors of size $m \times 1$ corresponding to the distances between the force points and the center of w_z force distribution.

Evaluating the function Π involves a large number of matrix–vector multiplications, while the optimization process requires a detailed analysis since the reliability of the output depends on the mathematical approach employed. All these requirements make the hardware implementation of the f search process a challenge given the real-time constraints of tactile sensing systems. To overcome these drawbacks, we propose a new approach to solve the system of Eq. (10) as described in the next sections.

3. Proposed approach and optimization process

The proposed model-driven contact force reconstruction method focuses on the relationship between the normal stress data (compression and traction stress) provided by the tactile sensor and the normal and tangential forces associated with the contact. Although this relationship was previously described in [7], in our approach the stress distribution becomes the key input information to establish the direction of the tangential force during the reconstruction process. This consideration simplifies the force reconstruction method by reducing the computational complexity to find the optimal values of μ_x and μ_y.

Fig. 2 presents the normal stress distribution for a Hertzian contact on a 10×10 sensor array. The shape of the normal stress surface in this figure is explained by the physics of the problem and the constraints given for a single static contact event. Normal stress magnitudes depend on the total force applied to the contact, while its signs hinge on the simultaneous effects of the normal and tangential forces. A negative

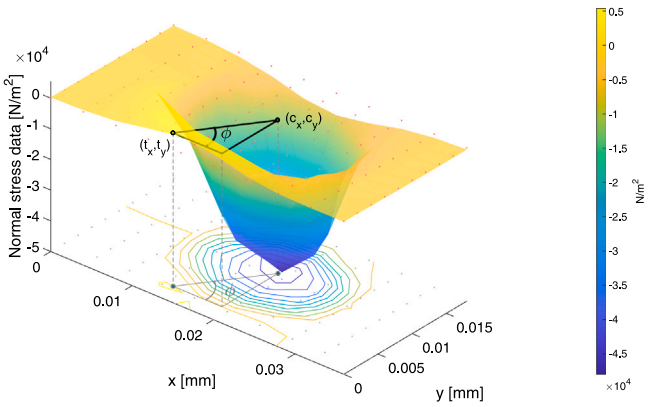

Fig. 2. A discrete normal stress distribution at the base of the sensor and identification of the centroids of stress and compression.

value in the normal stress (compression stress) is due to the action of normal forces, while a positive value (traction stress) is caused by the simultaneous effect of normal and tangential forces. The stress distribution allows identifying the centroid of the "compression zone" with coordinates (c_x, c_y) and the centroid of the "traction zone" with coordinates (t_x, t_y). The line joining these centroids gives the angle between the tangential forces ϕ,

$$\phi = \begin{cases} \tan^{-1}\left(\frac{c_y - t_y}{c_x - t_x}\right) & ; t_x < c_x \\ \\ \tan^{-1}\left(\frac{c_y - t_y}{c_x - t_x}\right) + 180° & ; t_x \geq c_x \end{cases} \tag{11}$$

In this scenario, if the tactile sensor data contains only compression components, it means that all sensor taxels report a stress value less than zero ($b_z(i) < 0$, $\forall i = 1, \ldots, m$) and that the contact is produced only by normal forces, meaning the problem can be univocally solved by equation Eq. (3).

This work proposes a new algorithm for the triaxial forces reconstruction, referred to as TFRA (Triaxial Forces Reconstruction Algorithm). This algorithm assumes that the resultant triaxial forces F_x, F_y, and F_z, are directly related to the angle ϕ. Resultant forces correspond to the summations of the contact force vectors for each axis and can be calculated from the linear functions system described in Eq. (10). Thus,

$$\begin{bmatrix} F_x \\ F_y \\ F_z \end{bmatrix} = \begin{bmatrix} \sum_{i=1}^{m} f_x(i) \\ \sum_{i=1}^{m} f_y(i) \\ \sum_{i=1}^{m} f_z(i) \end{bmatrix} = \begin{bmatrix} A_{10} + \mu_x A_{11} + \mu_y A_{12} \\ A_{20} + \mu_x A_{21} + \mu_y A_{22} \\ A_{30} + \mu_x A_{31} + \mu_y A_{32} \end{bmatrix} \tag{12}$$

where $A_{pq} = \sum_{i=1}^{m} a_{pq}(i)$.

Considering the physical characteristics of the contact analyzed, the resultant tangential forces depend directly on the resultant normal force, such that,

$$F_x = \mu F_z \cos\phi \tag{13}$$

$$F_y = \mu F_z \sin\phi \tag{14}$$

where μ is the contact friction coefficient, defined as,

$$\mu = \frac{\sqrt{F_x^2 + F_y^2}}{|F_z|} \tag{15}$$

Consequently, the quotient of tangential resultant forces can be estimated directly from ϕ as,

$$\frac{F_y}{F_x} = \tan\phi \tag{16}$$

This assignment has a significant impact on solving the system of linear functions defined in Eq. (10) since it reduces the number of

unknown variables in the system and simplifies the search process for variables μ_x and μ_x thanks to a linear dependence relationship between both variables. Hence, substituting Eq. (16) into Eq. (12), we find that,

$$\mu_x = \frac{A_{20} - A_{10}\tan\phi + \mu_y\left(A_{22} - A_{12}\tan\phi\right)}{A_{11}\tan\phi - A_{21}} \tag{17}$$

and,

$$\mu_y = \frac{A_{10}\tan\phi - A_{20} + \mu_x\left(A_{11}\tan\phi - A_{21}\right)}{A_{22} - A_{12}\tan\phi} \tag{18}$$

From these two equations, we can calculate one of the optimal variables μ_x or μ_y from a known value of ϕ, the constant parameters A_{pq} (defined by the geometry of the sensor), and the other optimal variable chosen as the independent variable. In any case, in this approach, it is assumed that these two variables are bounded in the range $[-1, 1]$ for the weight vector w in Eq. (8) to be consistent with the physics of the problem.

The TFRA offers a solution to the linear system of $3m$ equations Eq. (10), from the ϕ estimate Eq. (11), the assignment of the direction of tangential forces Eq. (16), and the linear dependence between μ_x and μ_y Eqs. (17) and (18). This algorithm simplifies the process of finding μ_x and μ_y and makes easier its implementation in real-time hardware platforms. Next Section 3.1 to Section 3.4 describe the four main stages of the TFRA: (i) estimate angle ϕ, (ii) select optimization variables μ_x or μ_y, (iii) find the optimal solution of Eq. (10), and (iv) scale the magnitudes of the forces.

3.1. Estimating the orientation of tangential forces

To estimate the centroids of the compression and tension zones, we will consider that the taxels of the compression zone are those with $b_z(i) < 0$, while the taxels of the traction zone are the ones for which $b_z(i) \geq 0$. Vectors $b_{z,c}$ and $b_{z,t}$ of size $m \times 1$, in compression and traction zones, respectively, are given by,

$$b_{z,c}(i) = \begin{cases} b_z(i) & ;\forall b_z(i) < 0 \\ 0 & ;\text{other case} \end{cases} \tag{19}$$

$$b_{z,t}(i) = \begin{cases} b_z(i) & ;\forall b_z(i) \geq 0 \\ 0 & ;\text{other case} \end{cases} \tag{20}$$

Using the definition proposed in [46] for the centroids calculation in a tactile image, we find,

$$\left(c_x, c_y\right) = \left(\frac{\sum_{i=1}^{m} b_{z,c}(i)\cdot p_x(i)}{\sum_{i=1}^{m} b_{z,c}(i)}, \frac{\sum_{i=1}^{m} b_{z,c}(i)\cdot p_y(i)}{\sum_{i=1}^{m} b_{z,c}(i)}\right) \tag{21}$$

$$\left(t_x, t_y\right) = \left(\frac{\sum_{i=1}^{m} b_{z,t}(i)\cdot p_x(i)}{\sum_{i=1}^{m} b_{z,t}(i)}, \frac{\sum_{i=1}^{m} b_{z,t}(i)\cdot p_y(i)}{\sum_{i=1}^{m} b_{z,t}(i)}\right) \tag{22}$$

where vectors p_x and p_y of size $m \times 1$ contain the information on the positions of the taxels with respect to the origin of the coordinate system. The ϕ estimate is therefore obtained by substituting equations Eq. (21) and Eq. (22) in Eq. (11).

3.2. Selecting the independent variable for the optimization process

The choice of w carried out in Eq. (8) comes from considering that each component, w_x, w_y, and w_z, has a distribution of values that is similar but not the same as for f_x, f_y, and f_z obtained in Eq. (10). Hence, although the quotient μ_y/μ_x does not coincide exactly with F_y/F_x, once $\tan(\phi)$ is known, we can know which of the two variables, μ_x or μ_y, is greater (in absolute value), since μ_y/μ_x is close to the value of $\tan(\phi)$. As mentioned above, the variable with the highest absolute value must in turn be limited to the intervals $[-1, 0]$ or $[0, 1]$, according to the value of ϕ. By selecting the variable of higher absolute value as independent (hereinafter μ_{ind}), we therefore ensure a reduced range ($[-1, 0]$ or $[0, 1]$ instead of $[-1, 1]$) for μ_{ind}, which simplifies the process of finding the optimal values of μ_x and μ_y. Fig. 3 shows the quadrants defined in the TFRA for selecting μ_{ind} in accordance with the value of ϕ.

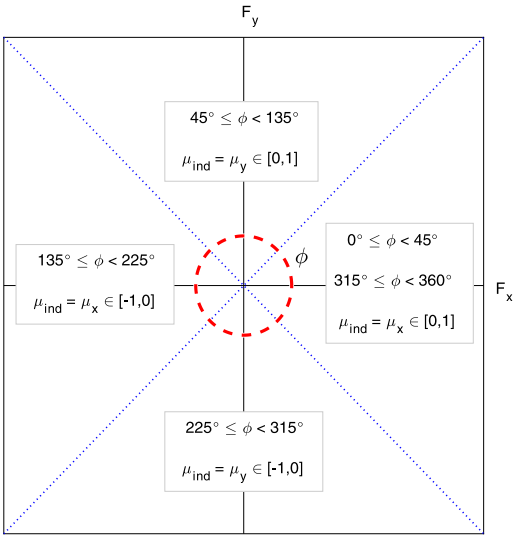

Fig. 3. Selection cases of the independent variable μ_{ind} for the optimization process.

3.3. Optimization process

The TFRA establishes that the distribution of forces $[f_x\ f_y\ f_z]^T$, has been reconstructed correctly if it meets the following two conditions related to the physics of the problem:

Condition 1. The normal forces are correctly reconstructed if when applied theoretically to the sensor, $[0\ 0\ f_z]^T$, only a compression effect is generated on the base of the sensor (no traction effect). Thus, when using $[0\ 0\ f_z]^T$ as force distribution in Eq. (3), the vector b_z^z, defined as $b_z^z = C_{33}\cdot f_z$, must satisfy:

$$B^z \equiv \sum_{i=1}^{m} b_z^z(i) = 0;\ b_z^z(i) > 0 \tag{23}$$

Condition 2. The tangential forces are correctly reconstructed if, when theoretically applied to the sensor, $[f_x\ f_y\ 0]^T$, they generate a distribution of traction values similar to the one actually obtained by the sensor. Thus, using $[f_x\ f_y\ 0]^T$ as the force distribution in Eq. (3), the vector b_z^{xy}, given by,

$$b_z^{xy} = \begin{bmatrix} C_{31} & C_{32} \end{bmatrix}\cdot\begin{bmatrix} f_x \\ f_y \end{bmatrix} \tag{24}$$

must satisfy,

$$B^{xy} \equiv \left|\sum_{i=1}^{m} b_z^{xy}(i) - \sum_{i=1}^{m} b_z(i)\right| = 0;\quad b_z^{xy}(i) > 0,\ b_z(i) > 0 \tag{25}$$

The optimal values of μ_x and μ_y are, therefore, those that generate a forces distribution closest to fulfillment of Eqs. (23) and (25). The two previous conditions generate two optimization functions that are much simpler than the ones used in the optimization process proposed in [7].

The TFRA consists of two independent search processes, one based on Eq. (23) and other based on Eq. (25). In the first one, the TFRA selects the smallest value of μ_{ind} (-1 or 0 denoted by μ_{ind}^0) at the initial iteration, and through Eq. (17) or Eq. (18) the TFRA finds the value of μ_x or μ_y (denoted μ_x^0 or μ_y^0).

Values of μ_x^0 and μ_y^0 are used for a first estimate of the forces distribution $[f_x^0\ f_y^0\ f_z^0]^T$. With f_z^0 we can determine the first value of the optimization function $B^{z,0}$. In the next iteration, we select $\mu_{ind}^1 = \mu_{ind}^0 + \Delta$, where Δ is an increment value defined for each iteration ($\Delta \ll 1$). After that, the TFRA proceeds in the same way as in the previous iteration. The process is repeated through to the maximum

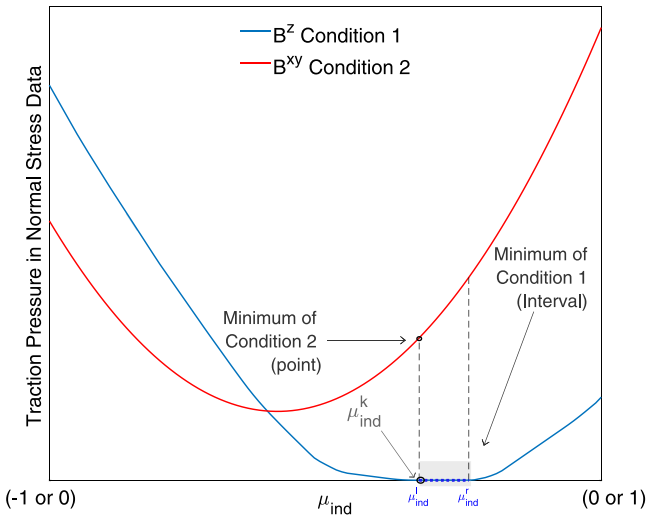

Fig. 4. Objective functions for the TFRA algorithm.

value of μ_{ind}. $B^z = B^z(\mu_{ind})$ is therefore evaluated for the entire range of μ_{ind}. An example of such a function is presented in blue in Fig. 4.

If a minimum value of B^z is reached, during the kth iteration, such a value is stored as $B^{z,k}$ along with the corresponding μ_x^k and μ_y^k. If only a single minimum has been found at the end of the search process, the optimal values of μ_x and μ_y, as well as the force distribution, are given by,

$$\mu_x = \mu_x^k \tag{26}$$

$$\mu_y = \mu_y^k \tag{27}$$

$$\begin{bmatrix} f_x^* & f_y^* & f_z^* \end{bmatrix}^T = \begin{bmatrix} f_x^k & f_y^k & f_z^k \end{bmatrix}^T \tag{28}$$

where $*$ indicates that the forces must be scaled (as shown in Section 3.4).

If there is more than a single minimum in B^z, as shown in Fig. 4, the ambiguity is solved with the second optimization process based on Eq. (25) (optimization is done in a similar way as already described). The existence of more than one global minimum in B^z is generally, due to discretization related to the number of sensors in the array.

An example of such an optimization process is highlighted in gray in Fig. 4. In the case of more than one global minimum in B^z, the optimal values of μ_x and μ_y are those that simultaneously provide a minimum value for B^z and the lowest value for B^{xy} in the interval of global minima of B^z.

3.4. Scaling contact forces

Once μ_x and μ_y have been found, the contact forces are scaled so that the modulus of the total force actually applied to the sensor, F_{sens}, matches the modulus of the distribution of forces, F^*, described in Eq. (28). Both force modules are given by,

$$F_{sens} = \sum_{i=1}^{m} |b_z(i)| \cdot (s_x \cdot s_y) \tag{29}$$

$$F^* = \sqrt{(F_x^*)^2 + \left(F_y^*\right)^2 + (F_z^*)^2} \tag{30}$$

The final stage of the TFRA corresponds to the assignment of,

$$\begin{bmatrix} f_x \\ f_y \\ f_z \end{bmatrix} = \frac{F_{sens}}{F^*} \cdot \begin{bmatrix} f_x^* \\ f_y^* \\ f_z^* \end{bmatrix} \tag{31}$$

4. Materials and methods

The validation of the TFRA was conducted by developing an experimental process similar to that presented in [7], for two cases of simple contacts (Hertzian and non-Hertzian) and using two different resolutions for the tactile sensors. For reference, we performed a series of simulations by means of the Finite Element Analysis (FEA) technique using Comsol Multiphysics® 6.0 to evaluate the proposed method and quantify the errors, determining the discretized normal stress in the taxels of the tactile sensor, b_z. TFRA was implemented using Matlab® R2020b with $\Delta = 0.01$ as step size for the μ_{ind} variation. Contacts with different angles of incidence of tangential forces were used for evaluation. Error analysis was carried out by comparing the resultant forces estimated by the TFRA with the forces obtained in the FEA simulation.

In the case of the Hertzian contact, an elliptical distribution of normal stress was applied to the base of the tactile sensor. The sensor was modeled as a rectangular solid of dimensions 40 mm × 20 mm × 3 mm, using an array of 10 × 10 taxels, and a resolution of $s_x = 4$ mm and $s_y = 2$ mm. For the non-Hertzian contact, a non-uniform normal stress rectangular distribution was applied on a sensor with dimension 40 mm × 40 mm × 3 mm, employing a array of 10 × 10 taxels and a resolution of $s_x = 4$ mm and $s_y = 4$ mm. The studied resolutions are in the range of commercially available tactile sensors, based on piezoelectric [47] and piezoresistive [48] technologies.

In both cases of contact, the origin of coordinates is established in the taxel T_1, (see Fig. 1). The q_z normal stress functions are defined in [42]. The tangential stress function depend on the coefficient of friction μ, and the orientation of tangential forces ϕ as,

$$\begin{bmatrix} q_x \\ q_y \end{bmatrix} = \mu q_z \begin{bmatrix} \cos\phi \\ \sin\phi \end{bmatrix} \tag{32}$$

The FEA carried out corresponds to a static study for a physical model of structural solid mechanics with the following properties for both contact cases:

Material characteristics. The isotropic properties of the material have a Young modulus $E = 1$ MPa, a Poisson relation $\nu = 0.48$, and a cover density $\rho = 1000$ Kg/m^3.

Boundary conditions. It is assumed a zero displacement constraint in the $XY-$plane for $z = 0$ (which acts as fixed support), and symmetry condition for the sensor sides.

Loads. The force loads q_z, q_x and q_y per unit of area were applied to the top sensor layer.

Mesh. An 'extremely fine' meshing parameter was applied, with an element size ranging from 0.008 mm and 0.8 mm.

A static and parametric study was carried out with the variation of ϕ and the coordinates of the center of the loads (x_0, y_0):

- Variation of ϕ in the range $[0°, 360°]$, with steps of 15°.
- Variation of the contact center (x_0, y_0) of the force distributions applied on the cover surface with displacements up to 50% of the sensor resolution, $\Delta x_0 = \pm 0.5 s_x$ and $\Delta y_0 = \pm 0.5 s_y$. Parameters $\mu = 0.5$ and $\phi = 45°$ were kept constant in all cases.

The performance parameters of the TFRA are the friction coefficient μ, the angle of orientation of the tangential forces ϕ, and the resultant triaxial forces F_x, F_y, and F_z obtained by applying equations Eqs. (12), (15) and (16) for each algorithm execution. Additionally, the stress surfaces estimated by the TFRA were also compared with the stress applied as a load for the FEA.

5. Results and discussion

The TRFA errors were calculated from the reference values generated by the FEA: μ_{ref}, ϕ_{ref}, and F_{ref}. Thus, errors in the μ and ϕ estimate are:

$$e(\mu) = 100 \frac{|\mu_{ref} - \mu|}{1.00}\% \tag{33}$$

Table 1
Contact force reconstruction for a Hertzian contact using the TFRA.

	Evaluated parameters	Analysis cases								
		TRFA								In [7]
		$\phi = 0°$	$\phi = 15°$	$\phi = 30°$	$\phi = 45°$	$\phi = 60°$	$\phi = 75°$	$\phi = 90°$	$\phi = 65°$	$\phi = 65°$
F_x	FEA [N]	2.86	2.77	2.48	2.03	1.43	0.74	0.00	1.21	1.22
	Algorithm [N]	2.51	2.73	2.61	2.21	1.76	0.94	−0.04	1.25	1.06
	$e(F_x)$[%]	5.94	0.54	2.13	3.15	5.54	3.41	0.62	0.71	2.78
F_y	FEA [N]	0.00	0.74	1.43	2.03	2.48	2.77	2.87	2.60	2.62
	Algorithm [N]	−0.08	0.58	1.23	1.87	2.43	2.87	2.99	2.44	2.28
	$e(F_y)$[%]	1.34	2.68	3.44	2.58	0.82	1.73	2.10	2.81	5.91
F_z	FEA [N]	−5.73	−5.73	−5.73	−5.73	−5.73	−5.73	−5.73	−5.73	−5.79
	Algorithm [N]	−5.35	−5.22	−5.17	−5.16	−5.09	−5.08	−5.10	−5.16	−5.17
	$e(F_z)$[%]	6.34	8.65	9.37	9.62	10.79	10.93	10.59	9.8	10.79
μ	FEA	0.50	0.50	0.50	0.50	0.50	0.50	0.50	0.5	0.5
	Algorithm	0.47	0.54	0.56	0.56	0.59	0.59	0.59	0.53	0.49
	$e(\mu)$[%]	3.03	3.60	5.70	6.18	8.97	9.41	8.57	3.08	1.00
ϕ	FEA [°]	0.00	15.00	30.00	45.00	60.00	75.00	90.00	65	65
	Algorithm [°]	−1.81	12.03	25.24	40.26	54.11	71.80	90.71	62.81	65
	$e(\phi)$[%]	0.50	0.82	1.32	1.32	1.64	0.89	0.20	0.61	0.00

The last column corresponds to the error estimate for the $\phi = 65°$ case reported in [7] by applying Eqs. (33) to (35).

Table 2
Contact force reconstruction for a non-Hertzian contact using the TFRA.

	Evaluated parameters	Analysis cases								
		TRFA								In [7]
		$\phi = 0°$	$\phi = 15°$	$\phi = 30°$	$\phi = 45°$	$\phi = 60°$	$\phi = 75°$	$\phi = 90°$	$\phi = 65°$	$\phi = 65°$
F_x	FEA [N]	3.39	3.27	2.93	2.40	1.69	0.88	0.00	1.43	1.43
	Algorithm [N]	3.14	3.31	3.20	2.35	1.38	0.53	−0.01	0.84	1.44
	$e(F_x)$[%]	3.30	0.53	3.62	0.67	4.17	4.65	0.09	7.84	0.14
F_y	FEA [N]	0.00	0.88	1.69	2.40	2.93	3.27	3.39	3.07	3.08
	Algorithm [N]	0.05	0.52	1.52	2.53	3.19	3.48	3.49	3.47	3.59
	$e(F_y)$[%]	0.60	4.77	2.36	1.78	3.40	2.76	1.42	5.44	7.32
F_z	FEA [N]	−6.78	−6.78	−6.78	−6.77	−6.77	−6.77	−6.77	−6.77	−6.79
	Algorithm [N]	−6.72	−6.62	−6.54	−6.63	−6.65	−6.64	−6.67	−6.56	−5.79
	$e(F_z)$[%]	0.79	2.12	3.12	1.91	1.71	1.73	1.40	2.69	14.36
μ	FEA	0.50	0.50	0.50	0.50	0.50	0.50	0.50	0.5	0.5
	Algorithm	0.47	0.51	0.54	0.52	0.52	0.53	0.52	0.55	0.60
	$e(\mu)$[%]	3.20	0.66	4.17	2.00	2.27	2.96	2.39	4.46	10.00
ϕ	FEA [°]	0.00	15.00	30.00	45.00	60.00	75.00	90.00	65	65
	Algorithm [°]	0.81	8.97	25.37	47.15	66.59	81.39	90.11	76.36	68.20
	$e(\phi)$[%]	0.23	1.67	1.29	0.60	1.83	1.77	0.03	3.16	0.88

The last column corresponds to the error estimate for the $\phi = 65°$ case reported in [7] by applying Eqs. (33) to (35).

$$e(\phi) = 100\frac{|\phi_{ref} - \phi|}{360°}\% \tag{34}$$

In the resultant forces case, the errors are relative to the modulus of the reconstructed resultant forces, so that:

$$e\left(F_{x,y,z}\right) = 100\frac{|F_{ref_{x,y,z}} - F_{x,y,z}|}{F_T}\% \tag{35}$$

where $F_T = \left(F_x^2 + F_y^2 + F_z^2\right)^{1/2}$.

5.1. Force estimation error due to variation of ϕ variation

Tables 1 and 2 show the results for the forces reconstruction for both types of contacts analyzed, when ϕ_{ref} varies between 0° and 90° (the other quadrants generate similar results). The last two columns of these tables present the performance comparison of the particular case reported in [7] when $\phi = 65°$.

In the Hertzian contact case, Table 1 shows a maximum error of 10.93% in the resultant forces reconstruction, 9.41% as the maximum error for the μ calculation, and 1.64% in the ϕ estimate (these errors include effects due to the sensor discretization). Comparing the TFRA results with [7] in both cases, all the parameters present values close to the FEA reference.

In the non-Hertzian contact case, Table 2 shows maximum errors of 5.44% in resultant forces reconstruction, 4.46% in the μ calculation, and 3.16% in the ϕ estimate. Compared to [7], the TFRA produces an improvement in the response of the resultant forces in the Y and Z-axes, even though it obtains a greater error in the reconstruction of the forces for the X-axis.

The resultant force errors for the proposed model are larger than those reported in [35] for a three-dimensional force reconstruction model. However, considering the simplicity of the TFRA as well as its independence on training routines or the transduction technologies employed, this method can be successfully applied to a broad range of tactile sensing systems.

The TFRA was validated using higher contact force levels than those reported by the data-driven triaxial approach presented in [13] (based on a multi-camera array for a resulting sensing surface of 49×51 mm^2), and lower than those reported in [12] (based on a non-array large-scale tactile sensor of 47×47 mm^2 active surface area). Despite this, the TFRA has not restrictions on the contact area size neither the forces magnitude to be estimated.

5.2. Variation on the tangential forces direction

Fig. 5 shows the TFRA response to the parametric variation of the orientation of the tangential force (ϕ_{ref}) in the range $[0°, 360°]$. For Hertzian and non-Hertzian contacts, it is observed that the algorithm outcomes closely follow the references established to μ and ϕ for all the experiments carried out.

Analyzing the Hertzian contact, Fig. 5(a) shows that μ is above μ_{ref} for most cases, while ϕ oscillates about the reference with a maximum error of 1.93%. For the non-Hertzian contact, Fig. 5(b) shows that μ oscillates about the reference, while ϕ follows the established FEA reference with a maximum error of 2.20%.

The above results indicate that the TFRA can detect variations in the orientation of the tangential forces and produce a coefficient of friction estimation close to the FEA reference model. Given that the two contact cases analyzed present significant differences in the contact area, size, and sensor resolution because of the parametric variation of ϕ_{ref}, it is observed that the proposed algorithm meets the generalization and scalability criteria defined in [26].

5.3. Reconstructing stress surfaces

Figs. 6 and 7 present the comparison between the stress surfaces applied as a load to the sensor and those reconstructed from the contact forces for four cases $\phi_{ref} = (0°, 30°, 60°, 90°)$ with $\mu_{ref} = 0.5$. Reference surfaces represent normal stress loads $q_{z,ref}$ from the FEA, while qt_{ref} relate to the modulus of the stress tangential components, such that,

$$qt_{ref} = \sqrt{q_{x,ref}^2 + q_{y,ref}^2} \tag{36}$$

Stress surfaces q_x, q_y, and q_z reconstructed by the TFRA are calculated from the triaxial components of the forces vector f and the sensor discretization, such that,

$$q_{x,y,z} = \frac{f_{x,y,z}}{s_x \cdot s_y} \tag{37}$$

Analyzing the orientation of tangential forces for $\phi_{ref} = 0°$ and $\phi_{ref} = 90°$ depicted in Figs. 6 and 7, it is observed that the stress surfaces depend only on the contribution of the force in one of the X or Y axes. Such behavior allows us to verify that the TFRA response is correct, since $F_y = 0$N for $\phi_{ref} = 0°$, and $F_x = 0$N for $\phi_{ref} = 90°$. Thus, the reconstructed stress surfaces are similar to those expected in all cases regardless of the value of ϕ_{ref}, the contact size, and the size and resolution of the sensor.

5.4. Variation of the contact centers

Fig. 8 shows the results of applying the TFRA to calculate μ and ϕ for displacements of the contact center for $\mu_{ref} = 0.5$, $\phi_{ref} = 45°$. The bottom of this figure shows the X-axis for the Hertzian contact, whereas the top shows the X-axis for the non-Hertzian contact. For the two types of contact analyzed, the values of μ and ϕ for the displacement $(0, 0)$ correspond to contacts completely centered in the sensor surface area, i.e., the stress components q_x, q_y and q_z have centers in (x_0, y_0). For the other eight displacement cases, the contact center is placed following a combination of X-axis or/ and Y-axis movements $(x_0 \pm \Delta x_0, y_0 \pm \Delta y_0)$. Considering that the scope of the proposed method covers only static contacts, the displacement cases analyzed correspond to independent contact events.

As observed in Fig. 8, the TFRA estimates μ and ϕ close to the references regardless of the contact center and contact surface shape. In the Hertzian contact, μ varies in the range $[0.50, 0.72]$ for values of ϕ in the range of $[36.61°, 43.41°]$; note that ϕ is oscillating under the reference. For the non-Hertzian contact, μ varies between $[0.52, 0.69]$ (which is above the reference) when ϕ is in the range $[28.81°, 58.91°]$, with a maximum error of 4.5% for all contacts. The more significant variations of μ and ϕ in the non-Hertzian case are due to the effects of the resolution and discretization of the tactile sensor over the sharp edges (discontinuities), which are characteristic of this kind of contact.

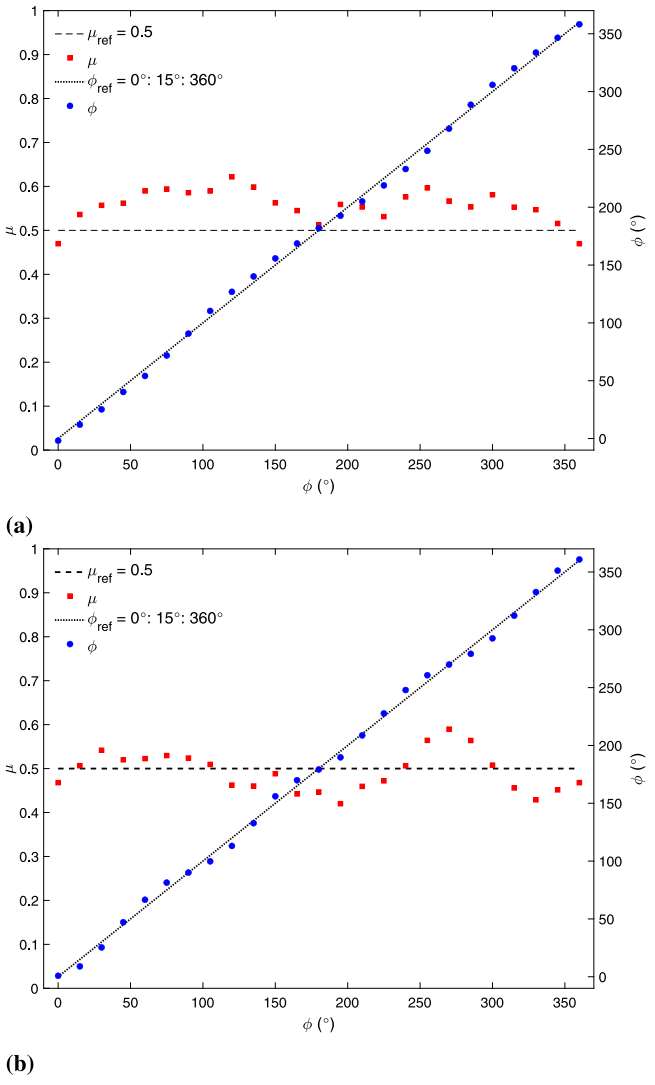

Fig. 5. Effect of parametric variation of ϕ_{ref} on the ϕ and μ estimate for: (a) Hertzian contact, (x_0, y_0) =(18 mm,9 mm); (b) non-Hertzian contact, (x_0, y_0) = (18 mm,18 mm).

5.5. Computational complexity and execution time

One advantage of the TFRA is that it does not require complex arithmetic operations, making its implementation in real-time tactile sensing systems easy. Most complex operations, such as higher-order matrix multiplications $(m\times3m)\cdot(3m\times m)$ and matrix inverse computation, required in Eqs. (6) and (9), are run offline as they only depend on the selected tactile sensor.

The TFRA optimal solution search algorithm has a computational complexity $O\left(m^2\right)$ with a single degree of freedom (μ_{ind}) for evaluating two stress functions that involve adds and matrix–vector multiplications of a maximum order $(m \times 2m) \cdot (2m \times 1)$, see Eqs. (23) and (25). These functions require only $m+1$ variables (f_z, μ_{ind}) for evaluating B^z and $2m+1$ variables (f_x, f_y, μ_{ind}) for evaluating B^{xy}.

Fig. 9 shows the comparison in the execution time for both software implementations, the TFRA, and our sequential implementation of the model proposed by [7]. These values were obtained by using the *timeit* Matlab® function [49], for $\mu = 0.5$ and ϕ changing in the range described in Section 4. The bottom of Fig. 9 presents a close-up of the temporal response for the TFRA. The maximum execution time in the case of the TFRA is 32.28 ms, and 27.13 ms for the Hertzian and non-Hertzian contacts, respectively, while our implementation of [7] reaches a maximum value of 264.39 ms and 821.70 ms,

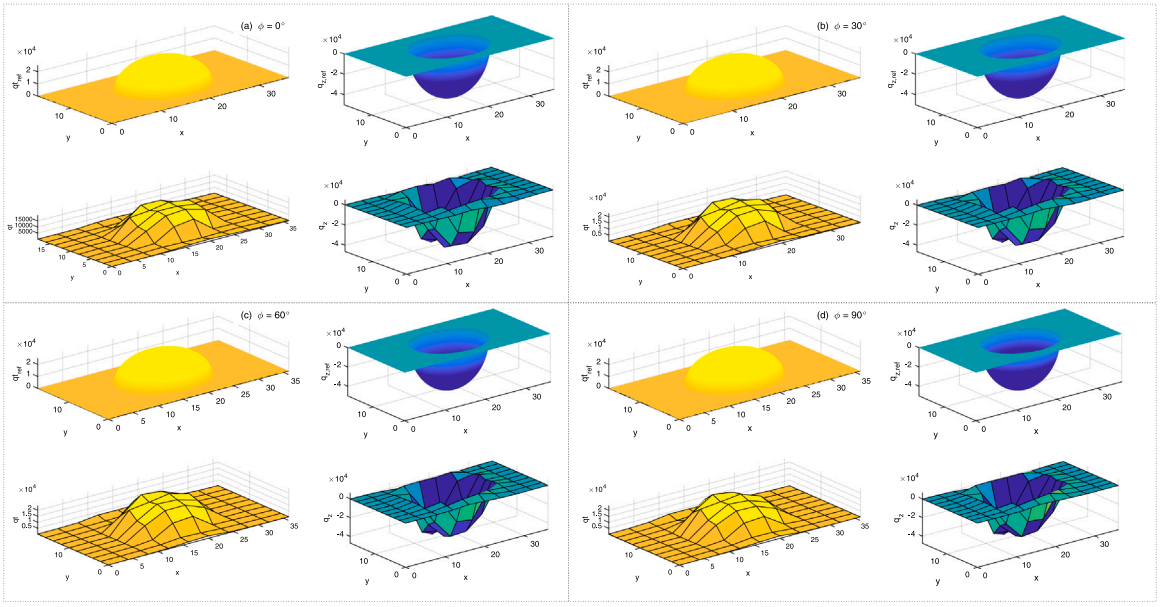

Fig. 6. Tangential and normal stress surfaces for the Hertzian contact. All magnitudes of qt_{ref}, $q_{z,ref}$, qt, and q_z stress functions are in N/m^2, while XY-axes in mm.

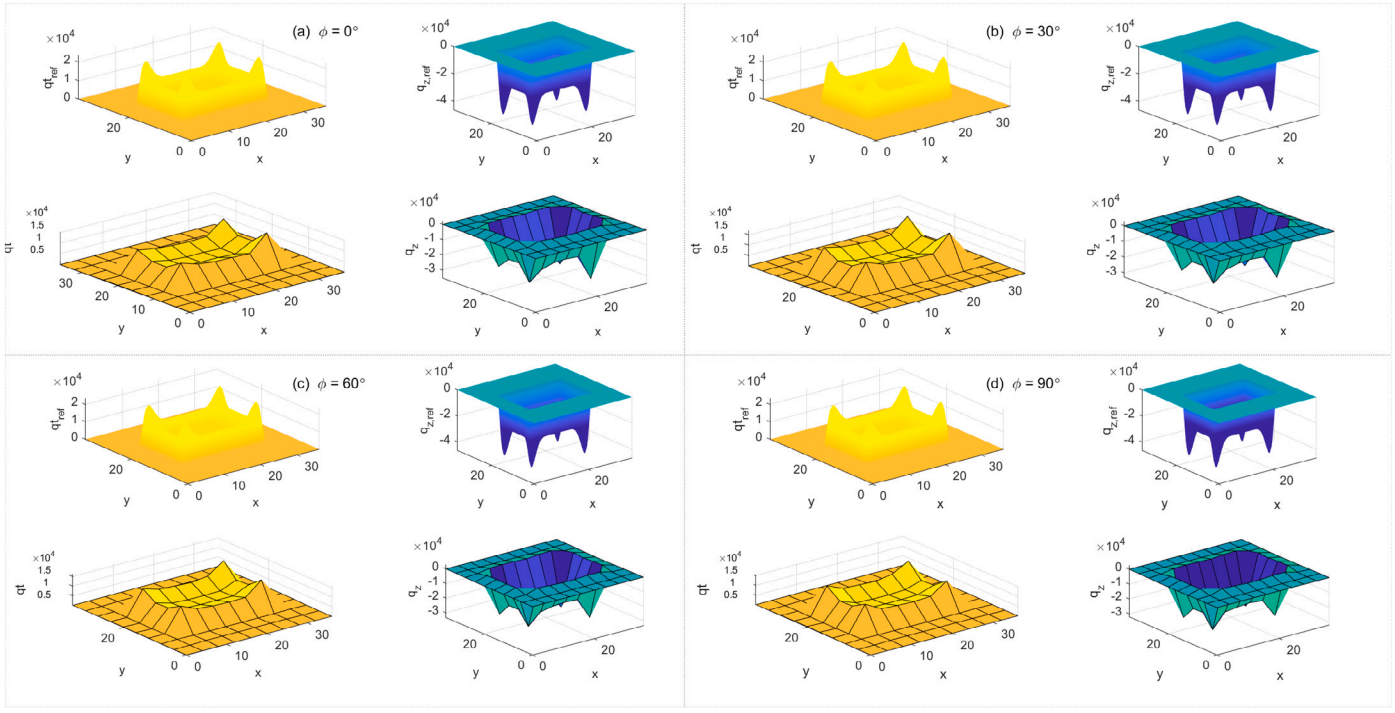

Fig. 7. Tangential and normal stress surfaces for the non-Hertzian contact. All magnitudes of qt_{ref}, $q_{z,ref}$, qt, and q_z stress functions are in N/m^2, while XY-axes in mm.

respectively. Although the TFRA presents a significant reduction in the execution time for the contact forces reconstruction, additional efforts could be made to improve these results in future real-time hardware implementation.

The bottom of Fig. 9 shows the upper limits for the response time of the TFRA, regardless of the type of contact, which ensures the predictability in the execution time proposed as an efficiency criterion by [26]. In addition, it is worth highlighting the reduction in the execution time of the proposed algorithm by requiring the sweep of a single independent variable (μ_{ind}) and not two (μ_x and μ_y) for the evaluation of the optimal functions.

6. Conclusions

This work presents a triaxial contact force reconstruction algorithm (TFRA) for tactile sensor arrays capturing discrete normal stress distributions on flat surfaces. TFRA is a model-driven method that proposes an alternative solution to the Boussinesq equation in ill-posed problems for single static contacts. This method represents an optimization of previous solutions reported in the literature, enhancing its implementation in real-time tactile sensing systems thanks to its arithmetic simplicity.

The TFRA estimates the orientation of the tangential forces of a contact event from the normal stress distribution information captured

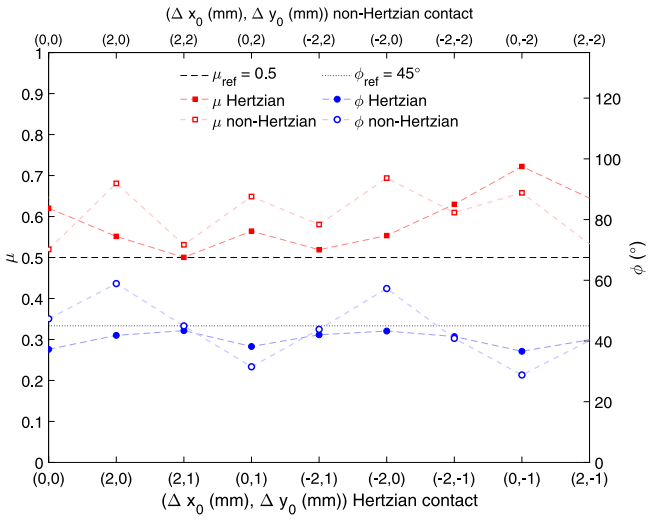

Fig. 8. Contact center displacement evaluation for the Hertzian contact with $(x_0, y_0) =$ (18 mm,9 mm), and non-Hertzian contact with $(x_0, y_0) =$ (18 mm,18 mm).

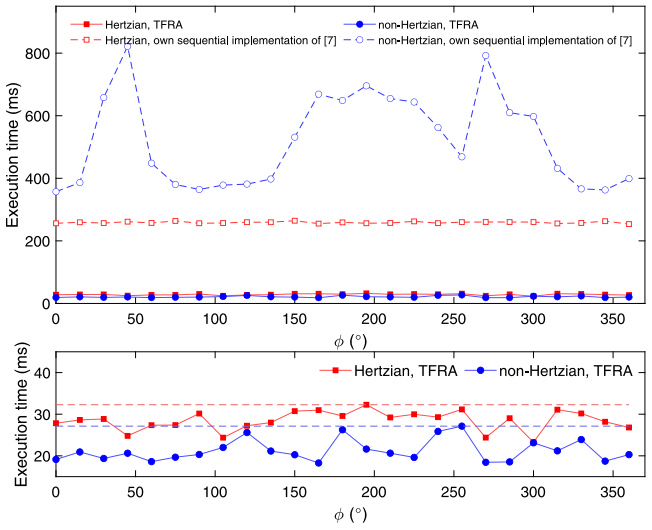

Fig. 9. Temporal response of the TFRA and our sequential implementation of the model proposed by [7].

by the sensor. Such estimation simplifies the process of searching for the optimal solution of the system by using two optimization functions that evaluate the effects of the reconstructed normal and tangential forces on discrete stress values calculated on the sensor surface. In this work, it is assumed that an optimal reconstruction of forces is the one that generates the normal stress distribution closest to the reference given by the sensor data.

Given the parametric variation of the orientation of the tangential forces and the displacement of the contact center, the proposed algorithm produced a maximum estimated error of 10.93% for Hertzian contacts on rectangular surfaces and 5.44% for non-Hertzian contacts on square surfaces. The error obtained depends on the initial estimate of the orientation of the tangential forces from the discrete normal stress data, which implies that it depends, in turn, on the size and number of taxels used. Thus, it is possible to state that increasing the sensor resolution (taxels/area) will improve the contact force reconstruction errors but will lengthen the execution time.

The proposed method reconstructs the triaxial forces independently of the smoothing of the edges of the contact object, the area and the center of the contact, and the discretization of the tactile array. This guarantees that the TFRA is generalizable, efficient, and scalable and makes its implementation feasible for real-time tactile decoding systems.

CRediT authorship contribution statement

María L. Pinto-Salamanca: Conceptualization, Methodology, Software, Validation, Data curation, Visualization, Investigation, Writing – review & editing. **Julián Castellanos-Ramos:** Conceptualization, Methodology, Software, Validation, Visualization, Writing – review & editing. **Wilson J. Pérez-Holguín:** Conceptualization, Methodology, Visualization, Investigation, Supervision, Writing – review & editing. **José A. Hidalgo-López:** Conceptualization, Methodology, Validation, Investigation, Supervision, Writing – review & editing, Funding acquisition.

Declaration of competing interest

The authors declare that they have no known competing financial interests or personal relationships that could have appeared to influence the work reported in this paper.

Funding

This work was partially supported by Universidad de Málaga-España, Gobierno de España Ministerio de Ciencia e Innovación [Contract PID2021-125091OB-I00], and Universidad Pedagógica y Tecnológica de Colombia [VIE DIN Convocatoria No 08-2021 SGI 3160].

Data availability

Data will be made available on request.

References

[1] Zou L, Ge C, Wang ZJ, Cretu E, Li X. Novel tactile sensor technology and smart tactile sensing systems: A review. Sensors 2017;17(11). http://dx.doi.org/10.3390/s17112653.

[2] Yang T, Xie D, Li Z, Zhu H. Recent advances in wearable tactile sensors: Materials, sensing mechanisms, and device performance. Mater Sci Eng R-Rep 2017;115:1–37. http://dx.doi.org/10.1016/j.mser.2017.02.001.

[3] Wang Y, Ding W, Mei D. Development of flexible tactile sensor for the envelop of curved robotic hand finger in grasping force sensing. Measurement: J Int Measur Confederation 2021;180(January):109524. http://dx.doi.org/10.1016/j.measurement.2021.109524.

[4] Ibrahim A, Pinna L, Valle M. Interface circuits based on FPGA for tactile sensor systems. In: 2017 new generation of CAS (NGCAS). 2017, p. 37–40. http://dx.doi.org/10.1109/NGCAS.2017.60.

[5] Oballe-Peinado Ó, Hidalgo-López JA, Sánchez-Durán JA, Castellanos-Ramos J, Vidal-Verdú F. Architecture of a tactile sensor suite for artificial hands based on FPGAs. In: 2012 4th IEEE RAS & EMBS international conference on biomedical robotics and biomechatronics. 2012, p. 112–7. http://dx.doi.org/10.1109/BioRob.2012.6290746.

[6] Gastaldo P, Pinna L, Seminara L, Valle M, Zunino R. A tensor-based approach to touch modality classification by using machine learning. Robot Auton Syst 2015;63(3, SI):268–78. http://dx.doi.org/10.1016/j.robot.2014.09.022.

[7] Seminara L, Capurro M, Valle M. Tactile data processing method for the reconstruction of contact force distributions. Mechatronics 2015;27:28–37. http://dx.doi.org/10.1016/j.mechatronics.2015.02.001.

[8] Lambeta M, Chou P-W, Tian S, Yang B, Maloon B, Most VR, et al. DIGIT: A novel design for a low-cost compact high-resolution tactile sensor with application to in-hand manipulation. IEEE Robot Autom Lett 2020;5(3):3838–45. http://dx.doi.org/10.1109/LRA.2020.2977257.

[9] Mohammadi A, Xu Y, Tan Y, Choong P, Oetomo D. Magnetic-based soft tactile sensors with deformable continuous force transfer medium for resolving contact locations in robotic grasping and manipulation. Sensors (Switzerland) 2019;19(22). http://dx.doi.org/10.3390/s19224925.

[10] Zhang B, Wang B, Li Y, Jin S. Magnetostrictive tactile sensor of detecting friction and normal force for object recognition. Int J Adv Robot Syst 2020;17(4). http://dx.doi.org/10.1177/1729881420932327.

[11] Li X, Li W, Zheng Y, Althoefer K, Qi P. Criminisi algorithm applied to a gelsight fingertip sensor for multi-modality perception. In: 2020 IEEE/ASME international conference on advanced intelligent mechatronics, vol. 2020-July. AIM 2020, Institute of Electrical and Electronics Engineers Inc.; 2020, p. 190–5. http://dx.doi.org/10.1109/AIM43001.2020.9158799.

[12] Cirillo A, Ficuciello F, Natale C, Pirozzi S, Villani L. A conformable force/tactile skin for physical human–robot interaction. IEEE Robot Autom Lett 2016;1(1):41–8. http://dx.doi.org/10.1109/LRA.2015.2505061.

[13] Trueeb C, Sferrazza C, D'Andrea R. Towards vision-based robotic skins: A data-driven, multi-camera tactile sensor. Institute for Dynamic Systems and Control, ETH Zurich, Switzerland: Institute of Electrical and Electronics Engineers Inc.; 2020, p. 333–8. http://dx.doi.org/10.1109/RoboSoft48309.2020.9116060.

[14] Acer M, Yıldız AF. Force localization estimation using a designed soft tactile sensor. In: Biosystems and biorobotics, vol. 22. Springer International Publishing; 2019, p. 8–12. http://dx.doi.org/10.1007/978-3-030-01887-0_2.

[15] Hellebrekers T, Chang N, Chin K, Ford M, Kroemer O, Majidi C. Soft magnetic tactile skin for continuous force and location estimation using neural networks. IEEE Robot Autom Lett 2020;1. http://dx.doi.org/10.1109/LRA.2020.2983707.

[16] De Maria G, Natale C, Pirozzi S. Force/tactile sensor for robotic applications. Sensors Actuators A 2012;175:60–72. http://dx.doi.org/10.1016/j.sna.2011.12.042.

[17] Kim D, Park Y-L. Contact localization and force estimation of soft tactile sensors using artificial intelligence. In: 2018 IEEE/RSJ international conference on intelligent robots and systems. IROS 2018, Institute of Electrical and Electronics Engineers Inc.; 2018, p. 7480–5. http://dx.doi.org/10.1109/IROS.2018.8593440.

[18] Chen H, Yang X, Wang P, Geng J, Ma G, Wang X. A large-area flexible tactile sensor for multi-touch and force detection using electrical impedance tomography. IEEE Sens J 2022;22(7):7119–29. http://dx.doi.org/10.1109/JSEN.2022.3155125.

[19] Polic M, Krajacic I, Lepora N, Orsag M. Convolutional autoencoder for feature extraction in tactile sensing. IEEE Robot Autom Lett 2019;4(4):3671–8. http://dx.doi.org/10.1109/LRA.2019.2927950.

[20] Zhang Z, Yimit A, Lu X, Hagihara Y. Design of a two-point-contact fingertip tactile force feedback device. In: 2017 2nd international conference on cybernetics, robotics and control. 2017, p. 71–4. http://dx.doi.org/10.1109/CRC.2017.49.

[21] Guo J, Shang C, Gao S, Zhang Y, Fu B, Xu L. Flexible plasmonic optical tactile sensor for health monitoring and artificial haptic perception. Adv Mater Technol 2023;8(7):2201506. http://dx.doi.org/10.1002/admt.202201506.

[22] Cramp S, Wallace B. Dynamic shear and normal forces on patient skin in sling lift transfers. In: 2021 IEEE international symposium on medical measurements and applications. 2021, p. 1–6. http://dx.doi.org/10.1109/MeMeA52024.2021.9478758.

[23] Wang L, Jones D, Chapman GJ, Siddle HJ, Russell DA, Alazmani A, Culmer P. Design of a digital triaxial force sensor for plantar load measurements. In: 2019 IEEE sensorS. 2019, p. 1–4. http://dx.doi.org/10.1109/SENSORS43011.2019.8956606.

[24] Kumar A, Rakesh Kumar RK, Shaikh MO, Lu C-H, Yang J-Y, Chang H-L, Chuang C-H. Ultrasensitive strain sensor utilizing a AgF–AgNW hybrid nanocomposite for breath monitoring and pulmonary function analysis. ACS Appl Mater Interfaces 2022;14(50):55402–13. http://dx.doi.org/10.1021/acsami.2c17756.

[25] He K, Zhao L, Yu P, Elhajj I, Xi N, Liu L. A flexible force tactile sensor array. In: 2020 10th Institute of Electrical and Electronics Engineers International conference on cyber technology in automation, control, and intelligent systems. 2020, p. 1–6. http://dx.doi.org/10.1109/CYBER50695.2020.9279192.

[26] Wasko W, Albini A, Maiolino P, Mastrogiovanni F, Cannata G. Contact modelling and tactile data processing for robot skins. Sensors 2019;19(4). http://dx.doi.org/10.3390/s19040814.

[27] Wei Q, Chen G, Pan H, Ye Z, Au C, Chen C, et al. Mxene-sponge based high-performance piezoresistive sensor for wearable biomonitoring and real-time tactile sensing. Small Methods 2022;6(2):2101051. http://dx.doi.org/10.1002/smtd.202101051.

[28] Duong LV, Ho VA. Large-scale vision-based tactile sensing for robot links: Design, modeling, and evaluation. IEEE Trans Robot 2021;37(2):390–403. http://dx.doi.org/10.1109/TRO.2020.3031251.

[29] Costanzo M, De Maria G, Natale C. Two-fingered in-hand object handling based on force/tactile feedback. IEEE Trans Robot 2020;36(1):157–73. http://dx.doi.org/10.1109/TRO.2019.2944130.

[30] Jiang X, Cheng Y, Bu J, Wei D. Application of BAS-BP model in 3D force decoupling of flexible tactile sensors. In: Z. Y, J. X, Z. T, editors. 3rd international conference on materials science, energy technology, power engineering, vol. 2154. MEP 2019, American Institute of Physics Inc.; 2019, http://dx.doi.org/10.1063/1.5125346.

[31] Chuang C-H, Weng H-K, Chen J-W, Shaikh MO. Ultrasonic tactile sensor integrated with TFT array for force feedback and shape recognition. Sensors Actuators A 2018;271:348–55. http://dx.doi.org/10.1016/j.sna.2018.01.022.

[32] Kalayeh KM, Charalambides PG. A non-linear model of an all-elastomer, in-plane, capacitive, tactile sensor under the application of normal forces. Sensors (Switzerland) 2018;18(11). http://dx.doi.org/10.3390/s18113614.

[33] Liang G, Mei D, Wang Y, Chen Z. Modeling and analysis of a flexible capacitive tactile sensor array for normal force measurement. IEEE Sens J 2014;14(11):4095–103. http://dx.doi.org/10.1109/JSEN.2014.2333472.

[34] Wu Z, Huang T, Hou C, Wang F, Liu H, Yang Z, et al. A flexible triaxial force capacitive sensor with microstructure electrode and orthogonal microstructure. In: 2021 IEEE international conference on manipulation, manufacturing and measurement on the nanoscale. 2021, p. 319–23. http://dx.doi.org/10.1109/3M-NANO49087.2021.9599733.

[35] Wang F, Song Y. Three-dimensional force prediction of a flexible tactile sensor based on radial basis function neural networks. In: Oddo CM, editor. J Sensors 2021;2021:8825019. http://dx.doi.org/10.1155/2021/8825019.

[36] Song Y, Wang F, Zhang Z. Decoupling research of a novel three-dimensional force flexible tactile sensor based on an improved BP algorithm. Micromachines 2018;9(5). http://dx.doi.org/10.3390/mi9050236.

[37] Castellanos-Ramos J, Navas-González R, Vidal-Verdú F. Tri-axial tactile sensing element. In: Tserepi A, Delgado-Restituto M, Makarona E, editors. Bio-MEMS and medical microdevices, vol. 8765. SPIE, International Society for Optics and Photonics; 2013, p. 87650P. http://dx.doi.org/10.1117/12.2016981.

[38] Cramp S, Maccoll C, Wallace RB. Preliminary results for novel shear force sensor using force sensitive resistors. In: 2020 IEEE international instrumentation and measurement technology conference. 2020, p. 1–6. http://dx.doi.org/10.1109/I2MTC43012.2020.9128858.

[39] Wang S, Huang K, Yang Y. A highly sensitive capacitive pressure sensor with microdome structure for robot tactile detection. In: 2019 20th international conference on solid-state sensors, actuators and microsystems & eurosensors XXXIII (Transducers & Eurosensors XXXIII). 2019, p. 458–61. http://dx.doi.org/10.1109/TRANSDUCERS.2019.8808583.

[40] Gao S, Weng L, Deng Z, Wang B, Huang W. Biomimetic tactile sensor array based on magnetostrictive materials. IEEE Sens J 2021;21(12):13116–24. http://dx.doi.org/10.1109/JSEN.2021.3068160.

[41] XELA Robotics Inc. XELA robotics sensing for the future. 2020, https://www.xelarobotics.com/index?lang=en. [Accessed 14 May 2022].

[42] Johnson KL. Contact mechanics. Cambridge: Cambridge University Press; 1985, http://dx.doi.org/10.1017/CBO9781139171731.

[43] Albert A. Regression and the moore-penrose pseudoinvers, vol. 94. 1972, p. 1–180.

[44] Boussinesq J. Application des potentiels à l'étude de l'équilibre et du mouvement des solides élastiques, vol. 4. Gauthier-Villars; 1885.

[45] Selvadurai AP. On Boussinesq's problem. Internat J Engrg Sci 2001;39(3):317–22. http://dx.doi.org/10.1016/S0020-7225(00)00043-4.

[46] Oballe-Peinado Ó, Hidalgo-López JA, Castellanos-Ramos J, Sánchez-Durán JA, Navas-González R, Herrán J, et al. FPGA-based tactile sensor suite electronics for real-time embedded processing. IEEE Trans Ind Electron 2017;64(12):9657–65. http://dx.doi.org/10.1109/TIE.2017.2714137.

[47] Seminara L, Pinna L, Valle M, Basiricò L, Loi A, Cosseddu P, et al. Piezoelectric polymer transducer arrays for flexible tactile sensors. IEEE Sens J 2013;13(10):4022–9. http://dx.doi.org/10.1109/JSEN.2013.2268690.

[48] Hidalgo-López JA, Oballe-Peinado Ó, Castellanos-Ramos J, Sánchez-Durán JA, Fernández-Ramos R, Vidal-Verdú F. High-accuracy readout electronics for piezoresistive tactile sensors. Sensors (Switzerland) 2017;17(11). http://dx.doi.org/10.3390/S17112513.

[49] MathWorks I. Measure time required to run function - MATLAB timeit - MathWorks. 2021, https://es.mathworks.com/help/matlab/ref/timeit.html. [Acessed 09 November 2022].

María L. Pinto-Salamanca is currently pursuing the Ph.D. degree in Mechatronics Engineering at Universidad de Malaga (UMA), and a Ph.D. in Engineering with an emphasis in Electronic Engineering at the Universidad Pedagógica y Tecnológica de Colombia (UPTC) under a joint supervision of doctoral tesis. Since 2011, she has been with the Electromechanical Engineering School, at UPTC. M. Pinto was a recipient of the L'ORÉAL-UNESCO For Women in Science 2021 Award, Colombia. Her main areas of research interests comprise tactile sensing, electronic design, biomedical and robotics systems.

Julián Castellanos-Ramos received the M.S. and Ph.D. degrees in industrial engineering from the Universidad de Malaga (UMA), Malaga, in 1999, and 2016, respectively. Since 2004, he has been with the Departamento de Electrónica, UMA. He is currently a member of the Instituto de Investigación Biomédica de Málaga (IBIMA). His current research interests include advanced tactile sensors, tactile interfaces, and applications in health and rehabilitation area.

Wilson J. Pérez-Holguín graduated in Electronic Engineering from the Universidad Pedagógica y Tecnológica de Colombia (UPTC) in 1999. He received an M.Sc. degree in Industrial Automation from the Universidad Nacional de Colombia in 2006 and a D.Eng. degree from Universidad del Valle, in collaboration with the Politecnico di Torino, in 2012. Since 2005, he has been with the School of Electronic Engineering at UPTC as an Associate Professor. He is also a professor of the Master of Engineering and the Doctorate in Engineering at UPTC. His research interests are the Design and Test of Microprocessors and Fault-Tolerant Systems, Parallel Computing, Tactile Sensing Systems, and Robotics.

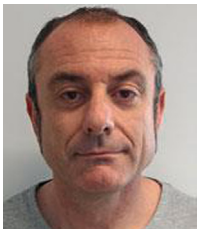

José A. Hidalgo-López received the M.Sc. degree in physics from the Universidad de Granada, Granada, Spain, in 1989, and the Ph.D. degree in microelectronics from the Universidad de Málaga (UMA), Málaga, Spain, in 1996. Since 1990, he has been with the Departamento de Electrónica, UMA, where he is currently an Associate Professor. He has authored or coauthored 30 articles in international indexed journals (JCR) and about 40 conference papers. His current research interests include electronics for sensors readout, 2-D resistive array sensors, signal processing using FPGAs, and computational arithmetic.